

# The impact of strain on the GeV-color center in diamond

Thijs G.I. van Wijk,<sup>1,2</sup> E. Aylin Melan,<sup>1</sup> Rani Mary Joy,<sup>2,3</sup> Emerick Y. Guillaume,<sup>1,2,4</sup>  
Paulius Pobedinskas,<sup>2,3</sup> Ken Haenen,<sup>2,3</sup> and Danny E. P. Vanpoucke<sup>1,2,\*</sup>

<sup>1</sup>Hasselt University, Institute for Materials Research (imo-imomec),  
Quantum & Artificial Intelligence design Of Materials (QuATOMs), Martelarenlaan 42, B-3500 Hasselt, Belgium

<sup>2</sup>imec, imo-imomec, Wetenschapspark 1, B-3590 Diepenbeek, Belgium

<sup>3</sup>Hasselt University, Institute for Materials Research (imo-imomec), Martelarenlaan 42, B-3500 Hasselt, Belgium

<sup>4</sup>University of Namur, Namur Institute of Structured Matter (NISM), Rue de Bruxelles 61, 5000 Namur, Belgium

Color centers in diamond, such as the GeV center, are promising candidates for quantum-based applications. Here, we investigate the impact of strain on the zero-phonon line (ZPL) position of GeV<sup>0</sup>. Both hydrostatic and linear strain are modeled using density functional theory for GeV<sup>0</sup> concentrations of 1.61 % down to 0.10 %. We present qualitative and quantitative differences between the two strain types: for hydrostatic tensile and compressive strain, red- and blue-shifted ZPL positions are expected, respectively, with a linear relation between the ZPL shift and the experienced stress. By calculating the ZPL shift for varying GeV<sup>0</sup> concentrations, a shift of 0.15 nm/GPa (0.38 meV/GPa) is obtained at experimentally relevant concentrations using a hybrid functional. In contrast, only red-shifted ZPL are found for tensile and compressive linear strain along the  $\langle 100 \rangle$  direction. The calculated ZPL shift exceeds that of hydrostatic strain by at least one order of magnitude, with a significant difference between tensile and compressive strains: 3.2 and 4.8 nm/GPa (8.1 and 11.7 meV/GPa), respectively. In addition, a peak broadening is expected due to the lifted degeneracy of the GeV<sup>0</sup>  $e_g$  state, calculated to be about 6 meV/GPa. These calculated results are placed in perspective with experimental observations, showing values of ZPL shifts and splittings of comparable magnitude.

## 1. INTRODUCTION

Over the last few decades, diamond color centers have been seen as promising candidates to fill in the role of single photon emitter for applications such as quantum cryptography[1], quantum computing[2, 3], and quantum sensing[4]. Color centers arise from defects (which can be missing atoms, impurity atoms, or combinations of both) which modify the optical properties of the crystal by introducing defect levels within the bandgap of the host material. The excitations to and from the defect levels can cause optical transitions, which give rise to a sharp zero-phonon line (ZPL) in the visible spectrum, hence giving color to an otherwise transparent material. Although color centers are not unique to diamond, this material is considered as the superior host for single photon emitters, as its indirect wide bandgap has the capacity to accommodate a wide variety of color centers[5, 6]. As of reporting this work, more than 500 diamond color centers have been identified[7], but only a small fraction have been characterized at the atomic-scale level. Less than 10 of these are considered to be bright and stable enough for a single photon emitter[6].

Color centers are often best categorized according to their coherence time, wavelength and Debye-Waller (DW) factor of their ZPL and quantum efficiency. This description makes for a great insight at the possible application of these materials: for instance, quantum communication applications require materials with bright and coherent optical transitions ensuring limited spectral diffusion

and with long coherence lifetimes[8–10].

One of the most extensively studied diamond color centers is the Nitrogen-vacancy (NV<sup>-</sup>) center. This color center has a long coherence time[11, 12], that would make it a potential material for quantum computing and quantum sensing applications[2], if it were not for its weak ZPL emission (DW factor of 0.03 [2, 13, 14]). Other color centers have also been investigated, such as the ones for which the impurity atom belongs to the group IV of the periodical table. They are considered to be promising candidates for quantum applications, since they show a bright ZPL emission[15–20]. Unlike the NV<sup>-</sup> color center, which has a  $C_{3v}$  point group, split-vacancy (XV) centers have  $D_{3d}$  symmetry, where the atom of element X (Si, Ge, Sn, or Pb) takes the interstitial position between two adjacent vacancies in diamond[21–25]. The resulting inversion symmetry protects the optical transitions from first-order electric field fluctuations, which limits the lifetime-broadening. This is the theoretical limit of the linewidth that can be achieved[26, 27].

The simplest group IV color center is the negatively charged Silicon-vacancy (SiV<sup>-</sup>) center. It has a strong ZPL with a weak sideband (DW factor of > 70 %) at room temperature, along with a very short lifetime ( $\approx 1$  ns)[16, 18]. However, it has been shown that it also has a low quantum efficiency and a sub-microsecond spin coherence time[8, 28, 29]. As a consequence, the other group-IV color centers, like the Germanium-vacancy (GeV) center, are receiving increasing interest.

The GeV<sup>-</sup> center shows similar optical properties as the SiV<sup>-</sup> center with regard to linewidth and DW factor since it has the same symmetry. However, due to its higher mass, GeV<sup>-</sup> has a larger ground state splitting,

\* Corresponding author: [Danny.Vanpoucke@UHasselt.be](mailto:Danny.Vanpoucke@UHasselt.be)

Table I. Brillouin zone sampling used for the different supercell calculations. The number of atoms in the pristine diamond supercells is given. The color center concentrations are defined as the ratio of GeV centers over C atoms in the system.

cell	atoms	conc.(%)	PBE relax	PBE & HSE06	ZPL
$c2 \times 2 \times 2$	64	1.61	$4 \times 4 \times 4$		$\Gamma$
$c3 \times 3 \times 3$	216	0.47	$2 \times 2 \times 3$		$\Gamma$
$c4 \times 4 \times 4$	512	0.20	$2 \times 2 \times 3$		$\Gamma$
$c5 \times 5 \times 5$	1000	0.10	$2 \times 2 \times 3$		$\Gamma$

resulting in a longer spin coherence time: in recent experiments, the quantum memory of the negatively charged  $\text{GeV}^-$  has even been extended to 20 ms[20, 30]. In addition, it also shows a higher quantum photoluminescence efficiency compared to  $\text{SiV}^-$ [31], making it an excellent candidate for quantum communication applications.

Another path that has been explored to increase the coherence time of split vacancy centers, is by using the neutrally charged centers instead of the negatively charged ones. The existence of the  $\text{SiV}^0$  and the  $\text{GeV}^0$  has been experimentally demonstrated by using electron spin resonance (ESR) measurement[32–34]. The  $\text{SiV}^0$  and  $\text{GeV}^0$  are effective spin  $S = 1$  systems[32]. Just like their negatively charged counterparts, they exhibit the same  $D_{3d}$  symmetry. Neutrally charged split-vacancies possess no partially filled degenerate energy levels in ground state, therefore these systems are not distorted by the dynamical Jahn-Teller effect. There may however be a product Jahn-Teller effect for the excited state configuration[35]. Their spin allows ESR at room temperature and coherent manipulation of spins. The  $\text{SiV}^0$  color center has been observed with a ZPL at 946 nm and a DW factor of 0.90 [36] It shows insensitivity to environmental decoherence and has a radiative lifetime of 1.8 ns[36]. Other neutral group IV color centers, are expected to possess similar valuable properties[11, 35]. In case of the  $\text{GeV}^0$  center a spectral line at 1.979 eV has been proposed as potential ZPL signature [37], though it was also associated with the vibrational sideband of  $\text{GeV}^-$ [38].

The present work addresses the characterization and determination of the energy levels of the  $\text{GeV}^0$  color center, which allows for a finer understanding of the observed effect of strain on the electronic structure of group IV-vacancy color centers, specifically on their ZPL[17, 39–41]. Strain is frequently observed as a result of diamond growth, and is especially pronounced in nanocrystalline diamond (NCD). In this paper, we investigate the impact of strain on the  $\text{GeV}^0$  center electronic structure, more specifically the shift of the  $\text{GeV}^0$  ZPL line by *ab initio* calculations. Based on these, we propose an interpretation of experimentally observed ZPL shifts for GeV centers, reported earlier by some of the authors.

## 2. METHODOLOGY

### 2.1. Computational Details

Density functional theory (DFT) calculations are performed using the Projector-Augmented-Wave formalism implemented in VASP.5.4.4 [42, 43]. The kinetic energy cutoff is set to 600 eV. The exchange and correlation behavior of the valence electrons (C:  $2s^22p^2$  and Ge:  $3d^{10}4s^24p^2$ ) is described using the generalized gradient approximation as devised by Perdew, Burke, and Ernzerhof (PBE) during atomic structure optimization and initial electronic structure calculations[44]. Within this work, the standard PBE GW-ready pseudo-potentials are used. Atomic positions and lattice parameters are optimized simultaneously during structure optimization using a conjugate gradient method with the energy convergence criterion set to  $1.0 \times 10^{-7}$ . After relaxation, the maximal forces remaining on any single atom are below  $0.53 \text{ meV}/\text{\AA}$ . Three structure optimization routes are considered in our work, relevant for the different strain models: (i) only ionic relaxation with the lattice parameter fixed at the PBE diamond bulk lattice parameter (3.5704  $\text{\AA}$ ), indicated as *Bulk*, (ii) ionic relaxation combined with a volume optimization—constrained to a cubic lattice—via a fit to the third order isothermal Birch-Murnaghan EOS, indicated as *Cubic*[45, 46], and (iii) a structure optimization allowing ionic positions, cell shape and volume to be optimized simultaneously, indicated as *Skewed*. For the linear and the hydrostatic strain models (*cf.*, Sec. 2.2.2), the *Bulk* and *Cubic* optimization routes are used, respectively.

The first Brillouin zone is sampled using an extended Monkhorst-Pack special  $k$ -point grid (*cf.*, Table I), selected—based on converges tests for the various system sizes—to have the total energy of the system converged to within 1 meV, and the forces on the atoms within  $1 \text{ meV}/\text{\AA}$ . Since local DFT functionals are known to underestimate the bandgap and the position of color center states in the bandgap, we use the corrected range-separated hybrid functional HSE06 for high accuracy electronic structure calculations[47–49]. However, as the computational cost of HSE06 in the systems investigated here is approximately between one and three orders of magnitude more expensive than PBE, no relaxation are conducted at the HSE06 level and the optimized structures obtained from PBE are used for HSE06 electronic structure calculations[50]. Since our focus lies with relative changes in electronic structure, the impact of the slight difference in lattice parameter is expected to be negligible. Furthermore, as DFT is only exact for the ground state of a system, the ZPL is considered as the required absorption energy for excitation, as such to remain within the validity of DFT. This approximation is further validated by the experimental observation that the absorption and emission spectra for the GeV are mirror images[51]. In addition, if one were to consider simulating emission, a Franck-Codon description would have

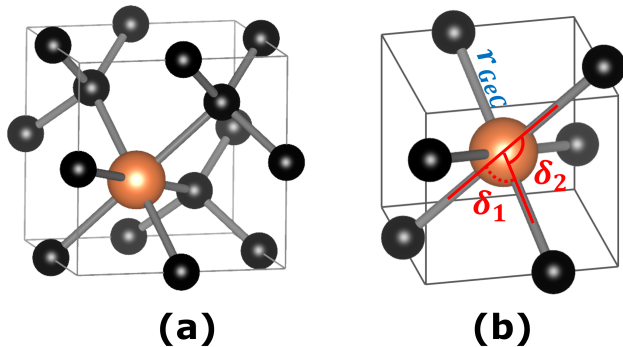


Figure 1. (a) Ball-and-stick representation of the GeV color center with split-vacancy structure in a  $2 \times 2 \times 2$  conventional supercell. The Ge atom is indicated in orange. (b) Local atomic structure of the GeV color center, showing the six-coordinated Ge, and the six surrounding C atoms. The two different angles,  $\delta_1$  and  $\delta_2$ , and bond length,  $r_{GeC}$ , are indicated.

to be adopted, which includes a relaxation of the excited state system (which falls outside of the purview of DFT). The associated relaxation energy, however, could be expected to be almost independent of the external strain, as the latter would only be able to slightly modify the hard diamond potential. As a result, its contribution to the relative ZPL position (or ZPL shift due to strain) would be negligible.

Within the field of quantum chemistry, several approaches have been devised to decompose the electron density into atomic charges[52, 53]. In this work, we use Hirshfeld-I charges[54–56], which have been shown to be very robust and to correlate well with formal charges[57, 58]. Atomic charges are obtained using the Hirshfeld-I partitioning scheme implemented for grid-based electron densities in the HIVE-code[55, 56, 59]. The convergence criterion for the iterative scheme is set to  $1.0 \times 10^{-5}$  electron. The charges are integrated on an atom-centered grid with logarithmic spacing in the radial directions (255 points) and spherical Lebedev-Laikov shells of 1202 grid-points[60, 61].

## 2.2. Color Center Model

The GeV<sup>0</sup> color center in diamond is modelled using conventional supercells of four different sizes:  $2 \times 2 \times 2$ ,  $3 \times 3 \times 3$ ,  $4 \times 4 \times 4$ , and  $5 \times 5 \times 5$ . In each supercell, two neighboring C atoms are removed and replaced by a single Ge atom (*cf.*, Fig. 1). Upon structure optimization, the Ge atom moves to a position corresponding to the center of the bond between the two former C atoms, which is why this defect is often referred to as a split-vacancy defect[23]. In its relaxed configuration, the Ge atom is six-coordinated and has a  $D_{3d}$  symmetry. Inspection of the electron density shows the presence of six covalent bonds, highlighting the fact that the single

Ge atom fills out all the available space. As Ge atoms are much larger than C atoms, the color center will locally strain the lattice.

In addition to local strain, two types of external strain are considered in this work as well: (i) hydrostatic strain and (ii) linear strain along the  $\langle 100 \rangle$  direction. Hydrostatic strain is modelled by modifying the system volume while retaining a cubic shape for the supercell (*i.e.*, *Cubic* optimization strategy). Five volumes are considered: 0,  $\pm 1$ , and  $\pm 2$  % with regard to the PBE equilibrium volume. The effective resulting strain for the different GeV<sup>0</sup> concentrations and functionals is obtained from the pressure-volume relation resulting from a third order isothermal Birch-Murnaghan equation-of-state (EOS) fit to the energy-volume data of the five points. Though the exact values vary slightly between the different systems, these five volumes span a pressure range of roughly 20 GPa. A first estimate of the equilibrium volume is obtained from the *Skewed* optimization strategy (with both shape and volume relaxed), while the final equilibrium volume is defined as the minimum of a third order isothermal Birch-Murnaghan equation-of-state EOS fit[45, 46]. For the linear strain along the  $\langle 100 \rangle$  direction, the equilibrium configuration is taken as a cubic cell with the PBE bulk diamond lattice parameter (3.5704 Å). In addition, four strained configurations are generated by stretching the  $\langle 100 \rangle$  lattice parameter by  $\pm 1$  and  $\pm 2$  %. The other two lattice parameters, however, are kept fixed (*i.e.*, *Bulk* optimization strategy). The resulting five energy-volume pairs are fitted using the same EOS, allowing for a comparable estimate of the experienced pressure.

## 2.3. Experimental Details

NCD films are grown using plasma-enhanced chemical vapor deposition (PECVD) on a 5 mm  $\times$  5 mm  $\times$  0.5 mm (100)-oriented Ge substrate. Ge acts both as the substrate and as the solid dopant source simultaneously[41]. The substrates are cleaned by an exposure to hydrogen plasma in the ASTeX 6500 microwave (MW) PECVD system. To create a high nucleation density, the cleaned substrates are seeded with a water-based detonation nanodiamond colloid by drop-casting, followed by a deionised water rinse and spin-drying steps[62]. The NCD film growth is carried out in the ASTeX 6500 MW PECVD system using a process gas mixture of 99 % hydrogen and 1 % methane with a total flow of 400 sccm. The working pressure and MW power are 45 Torr and 3000 W, respectively. The growth temperature is  $(720 \pm 20)^\circ\text{C}$ , measured using a dualwavelength Williamson Pro92 pyrometer. With these process conditions, a deposition time of 1 h leads to an NCD film thickness of 100 nm, monitored using the in-situ laser interferometry.

Room temperature photoluminescence (PL) measurements are carried out using Quantum Gem 532 laser with

532 nm wavelength and 1 mW power, focused via an objective with a numerical aperture of 0.95. For the GeV ZPL detection, a band-pass filter (ThorLabs FB600-10, center wavelength =  $(600 \pm 2)$  nm, Full Width Half Maximum =  $(10 \pm 2)$  nm) is used in the PL detection path for mapping.

### 3. RESULTS AND DISCUSSION

In the present work, three types of strain are considered: (a) local strain due to the presence of other defects, approximated via the color center concentration with the structures optimized using the *Bulk*, *Cubic* and *Skewed* optimization strategies, (b) hydrostatic strain, using the *Cubic* optimization strategy and (c) linear strain along the  $\langle 100 \rangle$  direction, using the *Bulk* optimization strategy.

#### 3.1. Color Center Concentration Effects

The impact of the color center concentration is studied through the comparison of supercells of different sizes: the small  $2 \times 2 \times 2$  supercell models a concentration of 1.61 %, whereas the larger  $5 \times 5 \times 5$  models a concentration 0.10 %. Although this is much larger than the usual experimentally observed concentrations for GeV centers, which is of the order of ppm or even ppb[19, 63, 64], the obtained results provide property trends that can be extrapolated towards the lower experimental concentrations. In addition, by considering three different sets of constraints during structure optimization (*cf.*, Sec. 2.2.2) further insight is gained in local strain effects.

Irrespective of the applied constraints and color center concentration, the relaxed structure presented the expected  $D_{3d}$  symmetry (*cf.*, Fig. 1b)[21–25]. As a result, the Ge atom in the color center acts as an inversion center (*cf.*, Table S.I), which makes the system less responsive to external electric fields since there is no permanent dipole moment. There is a rise in overlap of the excited states with the optical ground state, ensuring an improved ZPL intensity[26]. From Figs. 2a and b, it is clear that both the bond length and the angles in the color center ( $r_{GeC}$ ,  $\delta_1$  and  $\delta_2$  respectively, *cf.* Fig. 1b) depend on the concentration, as well as the constraints employed during structure optimization. For both, the trends are linear with concentration, with the results converging toward the same value for low concentrations. The different observed trends can be understood as a consequence of the applied constraints. For the *Bulk* systems, the lattice parameters are fixed on the PBE bulk lattice parameter, and as such, any structural relaxation involving a change in bond length is partially neutralized. It requires a sufficiently large supercell to have enough space for the C-C bonds between periodic copies of the color center to fully compensate for the distortion due to the Ge-C bonds (*i.e.* when the super cell is sufficiently large, the atoms furthest away from the GeV<sup>0</sup> center will have C-C

bonds closer to those of bulk diamond.). The same can be said for the *Cubic* systems, where the volume is optimized as well. However, in this case there is a slight overestimation due to the local distortion of the host lattice which requires a sufficiently large supercell to allow for C atoms in a non-distorted bulk environment. Extrapolating the Ge-C bond lengths to zero concentration gives 2.0315 Å for the *Bulk* and *Cubic* constrained systems, and 2.0309 Å for the *Skewed* system. This is significantly larger than the calculated C-C bond length in bulk diamond of 1.546 Å, and slightly smaller than the GeC bond length of 2.146 Å in the GeC<sub>6</sub>H<sub>18</sub> molecule. For the bond angles, it should be noted that the *Skewed* system no longer presents orthogonal lattice vectors, but lattice vectors at angles of 90.64° down to 90.04° at color center concentrations of 1.61 % and 0.10 %, respectively. Extrapolation to zero concentration results in the same angle pair under all three constraints: 94.42° and 85.58°. The volume of the color center is calculated as the difference between the optimized system volume and the volume of the pristine diamond bulk supercell. For systems with constrained lattice parameters (*Bulk*), the volume is by definition that of two C atoms. However, when the volume is relaxed as well, the color center volume increases to 16.9 Å<sup>3</sup>, or 2.97 times the volume of a single C atom. Note that for the *Skewed* systems the volume strongly reduces for increasing cell size. This is an artefact resulting from the presence of Pulay stresses. Although this effect is known to play a significant role in weakly bonded flexible systems like Metal Organic Frameworks[65], the small effect in the diamond systems at hand— 5 – 10 meV in total energy for the 1000 atom system—appears to be sufficient to artificially decrease the color center volume significantly. The *Cubic* systems on the other hand are obtained through an EOS-fit which does not suffer Pulay stresses, and thus presents the correct color center volume. Furthermore, in the latter case, a quickly converging result is obtained.

In addition to a local deformation of the host lattice, the GeV<sup>0</sup> center also gives rise to a significant redistribution of the local electron density. To quantify this redistribution, the Hirshfeld-I atomic charges are calculated for the different systems. As expected, the variations with regard to the GeV<sup>0</sup> concentration are small, and mainly a consequence of the variations in the bond lengths. To define the charge of the color center (not to be confused with the charge state), we consider the Ge atom and the six nearest neighbor C atoms. Charge oscillations in subsequent shells of C atoms quickly decay toward zero atomic charges. The Ge atom is found to be positively charged 1.61 electron, while all the nearest neighbor C atoms carry an identical negative charge of -0.60 electron, resulting in a total charge of the GeV<sup>0</sup> center -2.0 electron. These values are roughly independent of the GeV<sup>0</sup> concentration (*cf.*, Fig. S.7). The GeV<sup>0</sup> center appears to draw in significant additional charge from the host surrounding, and effect also seen in other point defects in diamond[66]. In comparison, we also calculate the



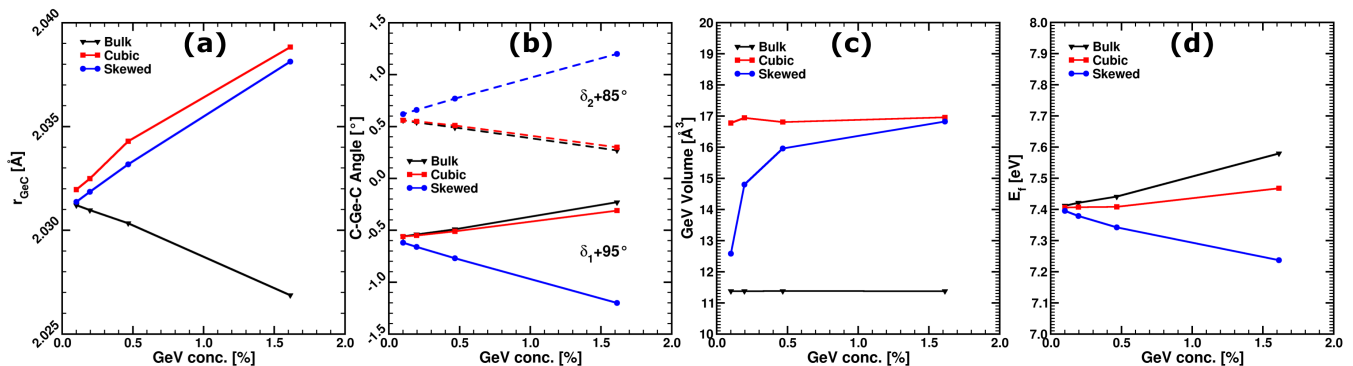


Figure 2. Structural properties of the GeV<sup>0</sup> color center, as a function of the concentration for the three different structure models: (a) the Ge-C bond length,  $r_{GeC}$ , (b) the complementary angles,  $\delta_1$  and  $\delta_2$ , and (c) the color center volume. (d) PBE-level formation energy of the GeV<sup>0</sup> center as function of concentration.

Hirshfeld-I charges for the GeV<sup>+</sup> and GeV<sup>-</sup> systems, using charged  $5 \times 5 \times 5$  supercells and manually set orbital occupancies. Total charges of  $-1.6$  and  $-2.7$  electron are found for GeV<sup>+</sup> and GeV<sup>-</sup>, respectively. This shows the GeV always draws in electrons from its surroundings, making it negatively charged. This is not to be confused with the GeV being in the negative charge state, which is recognized by the occupation of the GeV  $e_g$  states in the band gap.

The formation energy of the GeV<sup>0</sup> color center, as function of the concentration is presented in Fig. 2d, and is calculated as

$$E_f = E_{def} - N_C \mu_C - N_{Ge} \mu_{Ge}, \quad (1)$$

where  $E_{def}$  represents the total (PBE) energy of the system with the GeV<sup>0</sup> center,  $\mu_X$  the chemical potential and  $N_X$  the number of atoms of the respective atomic species present. The bulk energy in diamond configuration for both Ge and C is chosen as chemical potential, with the latter derived from a supercell of the same size as the supercell with the Ge<sup>0</sup> center, to have optimal compensation of errors. The results are well converged for the largest supercells, as seen in Fig. S.3, with the formation energy of the GeV<sup>0</sup> center being  $\sim 7.4$  eV for the three structure optimization strategies. Note that the differences between the three strategies show the structural impact of the color center to be rather long-ranged. The resulting strain energy can be considered to have a volumetric component and a shear component, leading to the differences between the *Cubic* and *Skewed* systems, with regard to the *Bulk* systems, respectively.

Although GeV and NV centers arise from the substitution of two carbon atoms by another element, the reconstruction of the atomic lattice results in different point group representations. The GeV color center, with  $D_{3d}$  symmetry has a higher symmetry than the NV with  $C_{3v}$  symmetry (which is a subgroup of the former), the most important difference being the inversion center at the Ge position. As a result, they exhibit different electronic structures, which can be derived from group theory.

Ge has four valence electrons in a  $4s^2 4p^2$  configuration, while the dangling bonds of the six neighboring C atoms contain one electron each, in one lobe of an  $sp^3$  hybridized orbital (*cf.*, Fig. S.1). The energy levels associated with the GeV color center in diamond are thus often considered as molecular orbitals constructed as a Symmetry-Adapted Linear Combination of Atomic Orbitals (SALC or Symmetry-Adapted LCAO) from the Ge atom valence orbitals and the dangling bonds of the six adjacent C atoms, based on the symmetry of the orbitals. The three lowest C related orbitals combine with the Ge orbitals and form pairs of bonding and anti-bonding combinations, while the  $e_g$  orbital is non-bonding. The molecular orbital diagram of the GeV<sup>0</sup> color center is shown in Fig. S.1e.

In contrast to this simplified picture, practical DFT calculations provide not only these one-electron orbitals, but all one-electron orbitals for all valence electrons in the system. The calculated Kohn-Sham (KS) energy levels at the  $\Gamma$ -point for the  $2 \times 2 \times 2$ - and  $5 \times 5 \times 5$ -supercells are presented in Fig. S.2. As the KS orbitals associated with the GeV<sup>0</sup> color center are expected to be localized on the Ge atom and its six surrounding C atoms, they can be identified based on their site-projected wave function character, and the knowledge of the theoretically predicted energy levels. To validate these results, the KS energy levels are also calculated for a minimal (passivated) cluster model of the color center: GeC<sub>6</sub>H<sub>18</sub>. When C and Ge atoms are constrained in the geometry of the embedded color center a similar picture of the positions of the GeV<sup>0</sup> color center states arises (*cf.*, Fig S.2), showing the theoretically expected degeneracy and orbital symmetries. Note that if this molecular cluster would be allowed to relax, the symmetry would increase to the  $O_h$  point group, in which a threefold degenerate state would be found below the highest occupied molecular orbital levels.

For the calculation of the ZPL, we consider excitations from the valence band maximum (VBM) to the empty  $e_g$  states of the GeV<sup>0</sup> located in the bandgap of diamond.

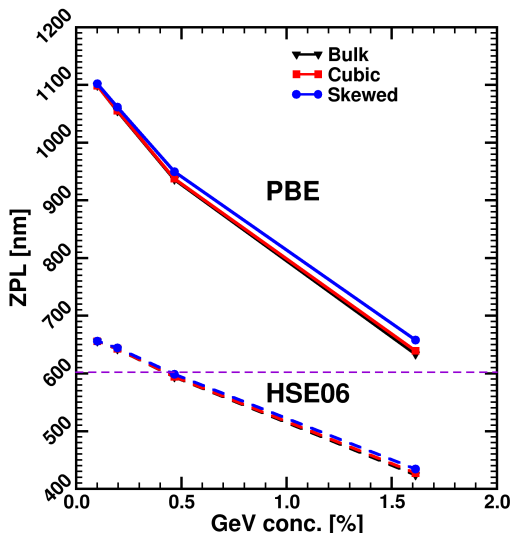


Figure 3. The calculated ZPL position, referenced to the VBM, as a function of the color center concentration for both PBE and HSE06 functionals. The dashed horizontal line indicates the position of the experimental value for the  $\text{GeV}^-$ .

The choice for the VBM instead of the  $e_u$  state is a consequence of the resonance between the VBM and the  $e_u$  state, located just below the VBM[25, 67, 68]. For comparison, we also calculated the ZPL positions using the  $e_u$  state as reference, which we will refer to as  $\text{ZPL}_{e_u}$  (*cf.* Fig. S.5). The ZPL is, by definition, a vertical excitation at the  $\Gamma$ -point of the first Brillouin zone, as no phonons carrying momentum are created.

The ZPL, calculated using the PBE and HSE06 functional, is shown in Fig. 3. The ZPL values are converged within 50 meV for the largest supercell (*cf.*, Fig. S.3). As can be seen, both functionals present the same linear relation as function of the  $\text{GeV}^0$  concentration. With the exception of the smallest supercell[69], all the HSE06 ZPL energies are shifted by 0.76 eV, compared to the PBE values. This constant shift of the ZPL values between different functionals may be an indication that actual physical behavior is presented. The strong dependence of the absolute position of the ZPL on the selected functional, however, causes this to be a difficult experimental parameter to predict theoretically. One should thus be careful with assignment based on calculations at a single concentration, for example, the HSE06 ZPL position from the  $3 \times 3 \times 3$  supercell fits the experimental ZPL position of the  $\text{GeV}^-$  rather nicely. Despite this limitation, the known quality relation between the functionals is also present[70]. The HSE06 results are shifted to lower wavelengths, compared to PBE, closer to the experimentally observed value of 602 nm for  $\text{GeV}^-$ . The overestimation of the ZPL position by the PBE functional is not unexpected, as it is well known that PBE (and local functionals in general) underestimate the bandgap as well as the position of states within the bandgap (*cf.*, Fig. S.4).

Although the concentrations considered are much higher than the experimental values (ppm range), the calculated shift of the ZPL as function of the  $\text{GeV}^0$  concentration is an indication that the proximity of  $\text{GeV}^0$  centers may give rise to a shift (or peak-broadening) in the spectrum of an ensemble of  $\text{GeV}^0$  centers.

As a final remark, let us briefly consider the impact of our choice of defining the ZPL as an excitation from the VBM. If one used the  $e_u$  state instead, a qualitatively similar picture arises with the ZPL shifted to lower wavelength (or higher energies). The resulting  $\text{ZPL}_{e_u}$  are shown in Fig. S.5. In addition, for low concentrations the trends become non-linear. This is a consequence of the non-linear shift of the position of the  $e_u$  state with regard to the VBM as function of the color center concentration (*cf.*, Fig. S.5c). In two additional calculations (PBE level, *Bulk* systems) using a  $6 \times 6 \times 6$  and  $7 \times 7 \times 7$  conventional supercell (0.06 and 0.04 %  $\text{GeV}^0$ ) the  $e_u$  state moves to a mere  $-299$  and  $-223$  meV below the VBM, from the  $-415$  meV at 0.1 %  $\text{GeV}^0$ . In contrast, for the 215 atom supercell (0.47 %  $\text{GeV}^0$ ) a value of  $-723$  meV is found, in excellent agreement with the value of  $-0.71$  calculated by Iwasaki and coworkers for the same system size and functional [64]. Also Goss and coworkers present a similar position of the  $e_u$  state using a 215 atom supercell and LSDA functional[23]. From these results, and the agreement with existing work, it appears that the  $e_u$  state shifts to the VBM for the  $\text{GeV}^0$  center in the dilute limit.

### 3.2. Hydrostatic Strain

To compare the effects of the strain at different  $\text{GeV}^0$  concentrations, the relative shift of the ZPL position,  $\Delta\text{ZPL}$ , (shown in Fig. 4) is chosen as indicator. The indicated pressure is obtained from the fitted third order Birch Murnaghan EOS, and offsets from zero for the equilibrium configuration are a consequence of the used methodology[71]. It is important to note that under hydrostatic strain, the symmetry is not altered, and as such the degeneracy of the  $e_g$  and  $e_u$  states is retained with a numerical accuracy of  $10^{-3}$  meV. This means no peak splitting or broadening is expected.

For all concentrations, and both functionals, a clear linear relation between  $\Delta\text{ZPL}$  and the experienced pressure is found. As the slope (*i.e.* pressure coefficient) is the same for compressive and tensile strain, a red-or blue-shift is expected, respectively. The pressure coefficient (or slope of the  $\Delta\text{ZPL}$ -pressure relation) depends on the  $\text{GeV}^0$  concentration as well as the functional (*cf.*, Fig. 4c). Note, however, that the different functionals do show the same qualitative picture. Based on the results of the larger supercells, the pressure coefficient can be extrapolated (*cf.*, Fig. 4c) to experimentally relevant concentrations, and is found to have a magnitude of 0.38 and 0.15 nm/GPa (or 0.32 and 0.38 meV/GPa, *cf.* Table S.II) for PBE and HSE06, respectively. For similar

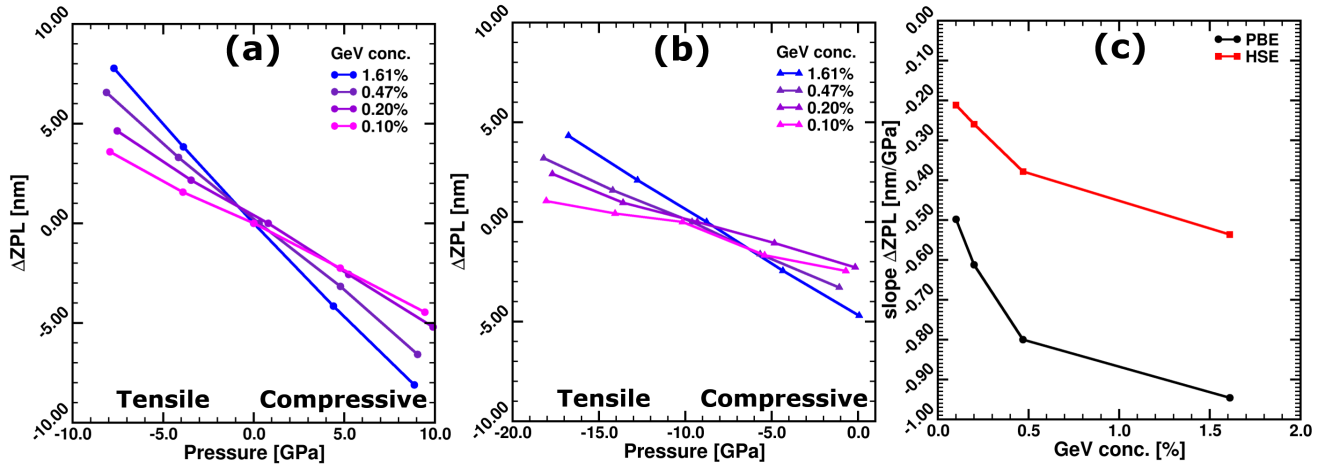


Figure 4. ZPL shift ( $\Delta ZPL$ ) under hydrostatic stress as a function of pressure, for different color center concentrations. Calculations are performed using the PBE (a) and HSE06 (b) functionals. The off-set from zero-pressure equilibrium for the HSE06 calculations is a consequence of the use of PBE optimized geometries[71]. The pressure is calculated from the EOS, with a positive and negative sign corresponding to compressed and expanded systems, respectively. For all calculations the middle point represents the equilibrium configuration. Points experiencing compressive or tensile stress are indicated for convenience. (c) The concentration dependent slope of the ZPL shifts (pressure coefficient) presented in (a) and (b).

work on the  $SiV^-$  color center, Lindner and coworkers[39] calculated, using a 512 atom supercell and the PBE functional, a pressure coefficient of the order of 1 nm/GPa is obtained for various stresses, in agreement with experimental ZPL shifts of 0.52 up to 4 nm/GPa. Specifically for the hydrostatic situation, the calculated pressure coefficient is of the order of 0.5 nm/GPa for stresses below 5.5 GPa, indicating the obtained values for  $GeV^0$  could be reasonable.

In the case that the  $e_u$  state is used as reference, the absolute values of the pressure coefficients increase by a factor of 2 – 3 (meV/GPa) or 1.5 – 2 (nm/GPa) (*cf.* Table S.II), but are expected to coincide in the dilute limit when  $e_u \rightarrow VBM$ .

Krivobok *et al.*[37] attributed a ZPL line at 1.979 eV (626 nm) to the  $GeV^0$  center in contrast to earlier work of the same group attributing it to the vibronic sideband of  $GeV^-$ . For this ZPL a pressure coefficient of 2.9 meV/GPa was measured, almost the same as for  $GeV^-$ . This value is higher than the calculated dilute limit value above, though it is well within the range of values calculated for the mid to high concentration cells. In comparison, Vindolet *et al.*[72] reported an experimental blue-shift of 2.7 meV/GPa ( $\sim 0.8$  nm/GPa[73]) under a hydrostatic pressure in the range of 20 to 40 GPa range for the  $GeV^-$  center. In the same work, these authors present a calculated value of 2.90 meV/GPa using the SCAN functional and a 512 atom supercell (0.2%  $GeV^-$ ), while Ekimov *et al.*[74] calculated a value of 3.1 meV/GPa for  $GeV^-$  using the HSE06 functional and non-conventional 88 and 233 atom supercells, 1.1 and 0.4 %  $GeV^-$ , respectively, also indicating a shift to smaller values with increasing cell size. These calculations, at single concentration points, where in agreement with the

experimentally obtained values for the  $GeV^-$  center, indicating the charge state to have a non-negligible influence.

The origin of the concentration dependence of the pressure coefficient (*cf.*, Fig. 4c) could be understood from a simple particle in a box model: the splitting between energy levels depends on the size of the box, with smaller boxes resulting in larger splittings. In the current case, the supercells are modified using the same relative change in lattice parameters, irrespective of their corresponding  $GeV^0$  concentrations. However, as we noted in the previous section, the local deformation of the host lattice due to the presence of the  $GeV^0$  center is long-ranged, and decays linearly with the  $GeV^0$  concentration. As such, within the particle in a box approximation of the  $GeV^0$  center, the change of the associated box size due to a relative change in the supercell size, will become less pronounced for the larger supercells as there is more room for both deformations to be accommodated. Therefore, lower concentration supercells also experience a smaller ZPL shift at the same pressure.

### 3.3. Linear Strain along the $\langle 100 \rangle$ Direction

Similar to the hydrostatic strain, the relative shift of the ZPL position,  $\Delta ZPL$ , is calculated under linear strain. This to allow for comparison between different  $GeV^0$  concentrations (*cf.*, Fig. 5). The indicated pressures are the result of third order Birch Murnaghan EOS fits to the Energy–Volume data resulting from the different linearly strained models[71]. In contrast to the hydrostatic case, the symmetry of the system is broken and reduced to a  $C_{2h}$  symmetry. As a result the

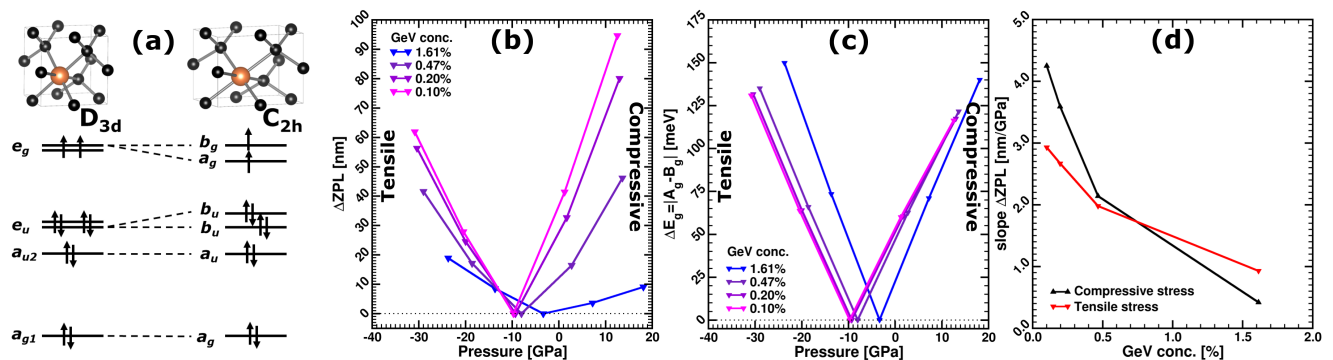


Figure 5. (a) Splitting of the  $\text{GeV}^0$  energy levels due to linear strain. Left: Theoretical energy levels for the  $\text{GeV}^0$  center in the  $D_{3d}$  symmetry. Right: Theoretical energy levels for the  $\text{GeV}^0$  center with linear strain applied along the  $\langle 100 \rangle$  direction, resulting in a  $C_{2h}$  symmetry. The initially degenerate energy levels in the  $D_{3d}$  symmetry, *i.e.*  $e_g$  and  $e_u$ , are split into  $a_g, b_g, a_u$  and  $b_u$ . The calculated  $\Delta ZPL$  (b) and level splitting (c) under linear strain, using the HSE06 functional, for different  $\text{GeV}^0$  concentrations[71]. (d) The pressure coefficient (*i.e.*, slope of  $\Delta ZPL$ ) as function of the  $\text{GeV}^0$  center concentration for both compressive and tensile stress, calculated using the HSE06 functional.

degeneracy of the  $e_g$  states is lifted, resulting in  $b_g$  and  $a_g$  states (*cf.*, Fig. 5a).

The shift of the ZPL due to tensile or compressive strains for the different  $\text{GeV}^0$  concentrations is presented in Fig. 5b for the HSE06 functional (results for PBE are given in SI). As for the hydrostatic case, the shift is more pronounced when the PBE functional is used, though the qualitative behavior is the same for both functionals, with the HSE06 results expected to be quantitatively more accurate. An important difference with the hydrostatic strain is that whereas the former converged to lower  $\Delta ZPL$  values for lower  $\text{GeV}^0$  concentrations, in the case linear strain, the convergence is toward a larger value. A second qualitative difference with the hydrostatic case is found in the fact that both tensile and compressive strain give rise to a red-shift. It is interesting to note that in case of the linear strain, the calculated pressure coefficient differs for tensile and compressive strain (*cf.*, Fig. 5d). Extrapolation to experimentally relevant  $\text{GeV}^0$  concentrations results in a red-shift of 3.2 or 4.8 nm/GPa (8.1 or 11.7 meV/GPa), for tensile and compressive stress, respectively. This is more than one order of magnitude stronger than for the hydrostatic case. This is in line with the results for the  $\text{SiV}^-$  color center, where also a larger pressure coefficient was calculated in case of a linear strain along  $\langle 100 \rangle$  compared to hydrostatic strain[39].

The theoretically expected splitting of the  $e_g$  state into the  $b_g$  and  $a_g$  states is also obtained from the DFT calculations (*cf.*, Fig. 5c and S.6b), and shows a comparable scale for PBE and HSE06. For both cases, the splitting behaves linear with the applied stress, with the results for HSE06(PBE) converging to 6.2(6.0) and 5.2(5.2) meV/GPa for tensile and compressive stress, respectively. Combined with the shift of the ZPL position, this splitting is expected to give rise to a deformation and peak broadening of the experimentally

observed ZPL line.

### 3.4. Experimental Observations and Theoretical Interpretation

Experimental studies carried out on NCD growth on Ge substrates have reported successful formation of  $\text{GeV}$  centers in diamond films[41, 75]. In our previous study, we reported the variation of the  $\text{GeV}$  ZPL position and attributed it to the residual stress in the NCD film (*cf.*, Fig. 6a)[41]. The remaining peaks observed in the spectrum (*e.g.*, Fig. 6b) may be surface-related or defects associated with nitrogen, but their exact origins have yet to be determined. This, however, falls outside of the scope of the current work.

Before drawing any comparisons with the DFT modelling, there are several important experimental observations to highlight when discussing the PL spectra of  $\text{GeV}$  centers. First, since Ge has a higher thermal expansion coefficient than diamond, a NCD film grown on a Ge substrate will experience a compressive residual stress once the sample is cooled down after high temperature diamond deposition. This compressive stress comes along with a tensile stress perpendicular to the substrate surface. For the growth conditions discussed in the experimental details, the in-plane residual compressive stress was estimated to be 0.85(15) GPa in magnitude and the out-of-plane tensile stress was estimated to be 0.21(3) GPa in magnitude[41]. Second, SEM images of the NCD film (100 nm thick) grown on a Ge substrate show that the diamond grains are randomly oriented[41]. Since the  $\text{GeV}$  center in diamond is always oriented along the  $\langle 111 \rangle$  direction, the apparent random orientation of the diamond grains in the NCD film will result in equally apparent randomly oriented  $\text{GeV}$  centers.



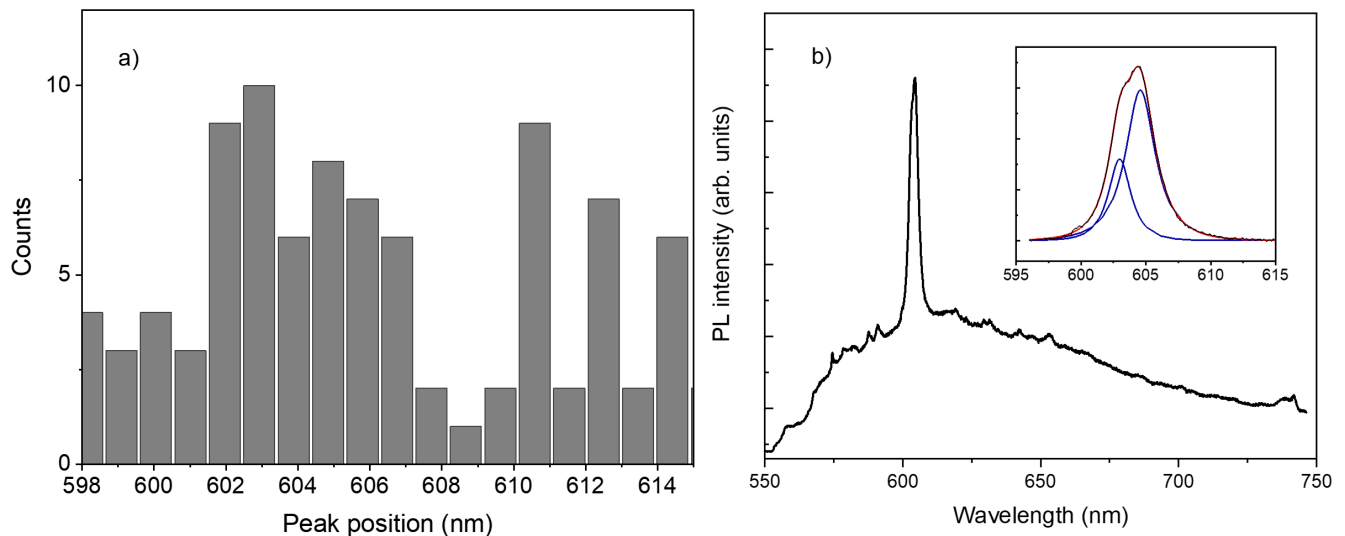


Figure 6. (a) Distribution of the PL positions and (b) an example of a room temperature PL spectrum of the NCD on Ge substrate. The inset shows a zoom-in of the GeV ZPL with two fitted peaks. Reused with permission from [41].

Third, the analysis of our previous work (*cf.* Fig. 6a), revealed the presence of both red- and blue-shifted ZPL (although with more observations of red-shifts than blue-shifts, the amplitude of the former being larger than the latter).

One example of a GeV spectrum is shown in Fig. 6b, with the most significant PL peak observed at about 604 nm. As is visible in the inset, the ZPL line has a clear shoulder and is formed by two contributions. The GeV ZPL is fitted to a Voigt function using Origin. The center wavelength position of the fitted peaks is located around 603.0(1) nm and 604.5(1) nm, which corresponds to an energy separation of about 5.1 meV. Considering the results of the linear strain model—theoretically calculated ZPL shift of about 3.2 nm/GPa and 4.8 nm/GPa (8.1 or 11.7 meV/GPa) for tensile and compressive stress, respectively—the observed ZPL shift of about 1 nm with regard to a non-strained GeV center corresponds to an experienced stress of less than 1 GPa. Considering the observed splitting, which also is part of the linear strain model, the observed 5.1 meV is in line with an experienced stress of 1 GPa or less. In addition, the larger splitting of the peak by about 1.5 nm is in qualitative agreement with the calculated HSE06 values for the linearly strained system, which also present a larger effect due to the splitting than the shift.

The spectrum presented in Fig. 6b can thus be understood as the result of a linearly strained system. However, as we discussed in the previous section, a linearly strained system gives rise to red-shifted ZPL for both compressive and tensile strain. In contrast, in Fig. 6a both red-shifted and blue-shifted ZPL may be present. Looking back at the two external strain models discussed in this work, the vector along the

GeV orientation behaves qualitatively different under hydrostatic and linear strain. In the case of hydrostatic strain, this vector will change in magnitude but not in orientation. In contrast, for the linear strain, this vector will change in orientation (breaking the symmetry). The in-plane aligned GeV centers experience an isotropic compressive stress (in the plane). This could be similar to the hydrostatic stress modelled above (depending on the orientation of the surrounding C atoms, the direction of the GeV orientation will only change in magnitude) and for compressive stress is predicted to give rise to blue-shifted ZPL. In contrast, note that for a linear compressive stress, a red-shifted ZPL is predicted. As such, this would clarify the observed blue-shifted ZPL in Fig. 6a. For an out-of-plane oriented GeV center an anisotropic strain will be experienced resulting in a breaking of the symmetry and a change in the orientation of the GeV (compared to the non-strained case). As such, a situation similar to the linearly strained GeV<sup>0</sup> center is observed. Depending on the exact orientation of the GeV and the ratio of the in-plane compressive and perpendicular tensile strain, both the compressive and tensile picture of the linear strain model come into play. However, as we noted, both give rise to red-shifted ZPL, be it with a different magnitude. Furthermore, the magnitude of these ZPL-shifts are shown to be much larger in the linear strain case than the hydrostatic strain case.

Considering Fig. 6a in detail, one notes there are more red-shifted cases than blue-shifted cases. This is in line with the expectation of a distribution of the GeV orientations. The exact nature of this distribution will influence the details of the observed ZPL shift distribution, but goes beyond the scope of the current work. Finally, the red-shifted ZPL go to larger values than the

blue-shifted cases, with a bimodal distribution for the former, which is in line with the expectations from the linear strain model showing a difference between tensile and compressive stress, while showing a stronger shift than hydrostatic strain.

#### 4. CONCLUSION

The impact of strain on the ZPL of the  $\text{GeV}^0$  color center in diamond is investigated using DFT, and compared to experimental observations. Three sources of local strain are considered: the proximity of other color centers, externally applied hydrostatic strain, and externally applied linear strain along the  $\langle 100 \rangle$  direction. For both the PBE and HSE06 functional the same qualitative linear relations between the ZPL position and color center concentration, as well as between the ZPL shift and the applied external strain are obtained. The former allows for extrapolation to experimentally relevant concentrations, though some deviation from the experimental value remains to be expected due to the choice of the functional, with higher rung functionals expected to approximate the experimental reality better. The observation of a concentration dependence of the ZPL position indicates one should be careful when proposing a direct link between the calculated ZPL position for one specific concentration and the values measured at ppm or ppb levels.

In the case of an externally applied strain, qualitatively different behavior is observed for different types of strain. Hydrostatic strain retains the color center symmetry, with the shift of the ZPL decreasing with decreasing  $\text{GeV}^0$  center concentration. Extrapolation of the obtained linear trend suggests both red- and blue-shifted

ZPL are expected for tensile and compressive strain, respectively. The size of the ZPL shift is the same for tensile and compressive stress, and extrapolation to experimental color center concentrations based on the calculated values is about 0.15(0.38) nm/GPa or 0.32(0.38) meV/GPa for HSE06(PBE) functional. In the case of linear strain along the  $\langle 100 \rangle$  direction, only red-shifted ZPL are expected. The extrapolated red-shift for experimentally relevant concentrations is an order of magnitude larger for the HSE06 calculations, namely about 3.2 and 4.8 nm/GPa (or 8.1 and 11.7 meV/GPa) for tensile and compressive stress, respectively. In addition to this much larger shift, the degeneracy of the  $e_g$   $\text{GeV}^0$  state is lifted, giving rise to a splitting between the two levels with a size of about 6 meV/GPa. Comparison to an experimentally observed GeV spectrum presents a qualitative agreement, supporting a symmetry breaking strain and showing a complex picture of significant variation of the strains experienced by individual GeV centers in NCD. Despite the inherent complexity present in the experimental sample and measurement, as well as the limitations present in first principles calculations, a qualitative understanding of the experimental observations can be obtained, providing a guide for future work.

#### ACKNOWLEDGEMENT

This work was financially supported by the Special Research Fund (BOF) via the BOF project R14181, the Methusalem NANO network, interuniversity BOF (BOF 23IU12), Research Foundation Flanders (FWO) projects G0D1721N and G0A0520N. The computational resources and services used in this work were provided by the VSC (Flemish Supercomputer Center), funded by the FWO and the Flemish Government–department EW1.

- 
- [1] N. Gisin, G. Ribordy, W. Tittel, and H. Zbinden, Quantum cryptography, *Rev. Mod. Phys.* **74**, 145 (2002).
  - [2] M. W. Doherty, N. B. Manson, P. Delaney, F. Jelezko, J. Wrachtrup, and L. C. Hollenberg, The nitrogen-vacancy colour centre in diamond, *Phys. Rep.* **528**, 1 (2013).
  - [3] F. Jelezko, T. Gaebel, I. Popa, M. Domhan, A. Gruber, and J. Wrachtrup, Observation of Coherent Oscillation of a Single Nuclear Spin and Realization of a Two-Qubit Conditional Quantum Gate, *Phys. Rev. Lett.* **93**, 130501 (2004).
  - [4] J. Hruby, M. Gulka, M. Mongillo, I. P. Radu, M. V. Petrov, E. Bourgeois, and M. Nesladek, Magnetic field sensitivity of the photoelectrically read nitrogen-vacancy centers in diamond, *Appl. Phys. Lett.* **120**, 162402 (2022).
  - [5] A. M. Zaitsev, Vibronic spectra of impurity-related optical centers in diamond, *Phys. Rev. B* **61**, 12909 (2000).
  - [6] I. Aharonovich, S. Castelletto, D. A. Simpson, C.-H. Su, A. D. Greentree, and S. Praver, Diamond-based single-photon emitters, *Rep. Prog. Phys.* **74**, 076501 (2011).
  - [7] A. Yelissev, S. Lawson, I. Sildos, A. Osvet, V. Nadolinny, B. Feigelson, J. Baker, M. Newton, and O. Yuryeva, Effect of HPHT annealing on the photoluminescence of synthetic diamonds grown in the Fe–Ni–C system, *Diam. Relat. Mater.* **12**, 2147 (2003).
  - [8] C. Bradac, W. Gao, J. Forneris, M. E. Trusheim, and I. Aharonovich, Quantum nanophotonics with group IV defects in diamond, *Nat. Commun.* **10**, 5625 (2019).
  - [9] E. Bersin, M. Sutula, Y. Q. Huan, A. Suleymanzade, D. R. Assumpcao, Y.-C. Wei, P.-J. Stas, C. M. Knaut, E. N. Knall, C. Langrock, N. Sinclair, R. Murphy, R. Riedinger, M. Yeh, C. Xin, S. Bandyopadhyay, D. D. Sukachev, B. Machielse, D. S. Levonian, M. K. Bhaskar, S. Hamilton, H. Park, M. Lončar, M. M. Fejer, P. B. Dixon, D. R. Englund, and M. D. Lukin, Telecom Networking with a Diamond Quantum Memory, *PRX Quantum* **5**, 010303 (2024).
  - [10] M. K. Bhaskar, R. Riedinger, B. Machielse, D. S. Levonian, C. T. Nguyen, E. N. Knall, H. Park, D. En-

- glund, M. Lončar, D. D. Sukachev, and M. D. Lukin, Experimental demonstration of memory-enhanced quantum communication, *Nature* **580**, 60 (2020).
- [11] D. Chen, N. Zheludev, and W. Gao, Building blocks for quantum network based on Group-IV Split-Vacancy centers in Diamond, *Adv. Quantum Technol* **3**, 1900069 (2020).
- [12] A. Beveratos, R. Brouri, T. Gacoin, J.-P. Poizat, and P. Grangier, Nonclassical radiation from diamond nanocrystals, *Phys. Rev. A* **64**, 061802 (2001).
- [13] D. Riedel, I. Söllner, B. J. Shields, S. Starosielec, P. Appel, E. Neu, P. Maletinsky, and R. J. Warburton, Deterministic Enhancement of Coherent Photon Generation from a Nitrogen-Vacancy Center in Ultrapure Diamond, *Phys. Rev. X* **7**, 031040 (2017).
- [14] H.-Q. Zhao, M. Fujiwara, and S. Takeuchi, Effect of substrates on the temperature dependence of fluorescence spectra of nitrogen vacancy centers in Diamond Nanocrystals, *Jpn. J. Appl. Phys.* **51**, 090110 (2012).
- [15] L. Razinkovas, M. W. Doherty, N. B. Manson, C. G. Van de Walle, and A. Alkauskas, Vibrational and vibronic structure of isolated point defects: The nitrogen-vacancy center in diamond, *Phys. Rev. B* **104**, 045303 (2021).
- [16] E. Neu, D. Steinmetz, J. Riedrich-Möller, S. Gsell, M. Fischer, M. Schreck, and C. Becher, Single photon emission from silicon-vacancy colour centres in chemical vapour deposition nano-diamonds on iridium, *New J. Phys.* **13**, 025012 (2011).
- [17] E. Neu, M. Fischer, S. Gsell, M. Schreck, and C. Becher, Fluorescence and polarization spectroscopy of single silicon vacancy centers in heteroepitaxial nanodiamonds on iridium, *Phys. Rev. B* **84**, 205211 (2011).
- [18] A. Dietrich, K. D. Jahnke, J. M. Binder, T. Teraji, J. Isoya, L. J. Rogers, and F. Jelezko, Isotopically varying spectral features of silicon-vacancy in diamond, *New J. Phys.* **16**, 113019 (2014).
- [19] Y. N. Palyanov, I. N. Kupriyanov, Y. M. Borzdov, and N. V. Surovtsev, Germanium: a new catalyst for diamond synthesis and a new optically active impurity in diamond, *Sci. Rep.* **5**, 14789 (2015).
- [20] P. Siyushev, M. H. Metsch, A. Ijaz, J. M. Binder, M. K. Bhaskar, D. D. Sukachev, A. Sipahigil, R. E. Evans, C. T. Nguyen, M. D. Lukin, P. R. Hemmer, Y. N. Palyanov, I. N. Kupriyanov, Y. M. Borzdov, L. J. Rogers, and F. Jelezko, Optical and microwave control of germanium-vacancy center spins in diamond, *Phys. Rev. B* **96**, 081201 (2017).
- [21] C. Hepp, T. Müller, V. Waselowski, J. N. Becker, B. Pingault, H. Sternschulte, D. Steinmüller-Nethl, A. Gali, J. R. Maze, M. Atatüre, and C. Becher, Electronic Structure of the Silicon Vacancy Color Center in Diamond, *Phys. Rev. Lett.* **112**, 036405 (2014).
- [22] J. P. Goss, R. Jones, S. J. Breuer, P. R. Briddon, and S. Öberg, The Twelve-Line 1.682 eV Luminescence Center in Diamond and the Vacancy-Silicon Complex, *Phys. Rev. Lett.* **77**, 3041 (1996).
- [23] J. P. Goss, P. R. Briddon, M. J. Rayson, S. J. Sque, and R. Jones, Vacancy-impurity complexes and limitations for implantation doping of diamond, *Phys. Rev. B* **72**, 035214 (2005).
- [24] J. P. Goss, P. R. Briddon, and M. J. Shaw, Density functional simulations of silicon-containing point defects in diamond, *Phys. Rev. B* **76**, 075204 (2007).
- [25] G. Thiering and A. Gali, Ab initio Magneto-Optical Spectrum of Group-IV vacancy Color centers in Diamond, *Phys. Rev. X* **8**, 021063 (2018).
- [26] M. Ruf, N. H. Wan, H. Choi, D. Englund, and R. Hanson, Quantum networks based on color centers in diamond, *J. Appl. Phys.* **130**, 070901 (2021).
- [27] M. K. Bhaskar, D. D. Sukachev, A. Sipahigil, R. E. Evans, M. J. Burek, C. T. Nguyen, L. J. Rogers, P. Siyushev, M. H. Metsch, H. Park, F. Jelezko, M. Lončar, and M. D. Lukin, Quantum Nonlinear Optics with a Germanium-Vacancy Color Center in a Nanoscale Diamond Waveguide, *Phys. Rev. Lett.* **118**, 223603 (2017).
- [28] L. J. Rogers, K. D. Jahnke, M. H. Metsch, A. Sipahigil, J. M. Binder, T. Teraji, H. Sumiya, J. Isoya, M. D. Lukin, P. Hemmer, and F. Jelezko, All-Optical Initialization, Readout, and Coherent Preparation of Single Silicon-Vacancy Spins in Diamond, *Phys. Rev. Lett.* **113**, 263602 (2014).
- [29] B. Pingault, J. N. Becker, C. H. H. Schulte, C. Arend, C. Hepp, T. Godde, A. I. Tartakovskii, M. Markham, C. Becher, and M. Atatüre, All-Optical Formation of Coherent Dark States of Silicon-Vacancy Spins in Diamond, *Phys. Rev. Lett.* **113**, 263601 (2014).
- [30] K. Senkalla, G. Genov, M. H. Metsch, P. Siyushev, and F. Jelezko, Germanium vacancy in diamond quantum memory exceeding 20 ms, *Phys. Rev. Lett.* **132**, 026901 (2024).
- [31] X. Tan, W. Shao, X. Ma, Z. He, B. Zhang, C. Chen, Y. Ren, and S. Sun, Theoretical study on the formation of diamond germanium vacancy color center, *Surf. Sci.* **715**, 121950 (2022).
- [32] A. M. Edmonds, M. E. Newton, P. M. Martineau, D. J. Twitchen, and S. D. Williams, Electron paramagnetic resonance studies of silicon-related defects in diamond, *Phys. Rev. B* **77**, 249901 (2008).
- [33] U. F. S. D'Haenens-Johansson, A. M. Edmonds, M. E. Newton, J. P. Goss, P. R. Briddon, J. M. Baker, P. M. Martineau, R. U. A. Khan, D. J. Twitchen, and S. D. Williams, EPR of a defect in CVD diamond involving both silicon and hydrogen that shows preferential alignment, *Phys. Rev. B* **82**, 155205 (2010).
- [34] A. Komarovskikh, M. Uvarov, V. Nadolinny, and Y. Palyanov, Spin relaxation of the Neutral Germanium-Vacancy Center in Diamond, *phys. Status Solidi (a)* **215**, 1800193 (2018).
- [35] G. Thiering and A. Gali, The  $(e_g \otimes e_u) \otimes E_g$  product Jahn-Teller effect in the neutral group-IV vacancy quantum bits in diamond, *npj Comput. Mater.* **5**, 18 (2019).
- [36] B. C. Rose, D. Huang, Z.-H. Zhang, P. Stevenson, A. M. Tyryshkin, S. Sangtawesin, S. Srinivasan, L. Loudin, M. L. Markham, A. M. Edmonds, D. J. Twitchen, S. A. Lyon, and N. P. De Leon, Observation of an environmentally insensitive solid-state spin defect in diamond, *Science* **361**, 60 (2018).
- [37] V. S. Krivobok, E. A. Ekimov, S. G. Lyapin, S. N. Nikolaev, Y. A. Skakov, A. A. Razgulov, and M. V. Kondrin, Observation of a 1.979-eV spectral line of a germanium-related color center in microdiamonds and nanodiamonds, *Phys. Rev. B* **101**, 144103 (2020).
- [38] Y. Makino, Y. Saito, Y. Minowa, A. Tsurui, Y. Kishino, T. Kouuchi, Y. Takeuchi, G. Yamagishi, and M. Ashida, Optical properties of negatively charged germanium-vacancy centers in detonation nanodiamonds with an average single-digit nanometer particle size, *Jpn. J. Appl.*

- Phys.* **63**, 035003 (2024).
- [39] S. Lindner, A. Bommer, A. Muzha, A. Krueger, L. Gines, S. Mandal, O. Williams, E. Londero, A. Gali, and C. Becher, Strongly inhomogeneous distribution of spectral properties of silicon-vacancy color centers in nanodiamonds, *New J. Phys.* **20**, 115002 (2018).
- [40] S. A. Grudinkin, N. A. Feoktistov, M. A. Baranov, A. N. Smirnov, V. Y. Davydov, and V. G. Golubev, Low-strain heteroepitaxial nanodiamonds: fabrication and photoluminescence of silicon-vacancy colour centres, *Nanotechnol.* **27**, 395606 (2016).
- [41] R. Mary Joy, P. Pobedinskas, E. Bourgeois, T. Chakraborty, J. Goerlitz, D. Herrmann, C. Noel, J. Heupel, D. Jannis, N. Gauquelin, J. D’Haen, J. Verbeeck, C. Popov, L. Houssiau, C. Becher, M. Nesládek, and K. Haenen, Photoluminescence of Germanium-Vacancy Centers in Nanocrystalline Diamond Films: Implications for Quantum Sensing Applications, *ACS Appl. Nano Mater.* **7**, 3873 (2024).
- [42] G. Kresse and J. Furthmüller, Efficient iterative schemes for ab initio total-energy calculations using a plane-wave basis set, *Phys. Rev. B* **54**, 11169 (1996).
- [43] G. Kresse and D. Joubert, From ultrasoft pseudopotentials to the projector augmented-wave method, *Phys. Rev. B* **59**, 1758 (1999).
- [44] J. P. Perdew, K. Burke, and M. Ernzerhof, Generalized Gradient Approximation Made Simple, *Phys. Rev. Lett.* **77**, 3865 (1996).
- [45] F. Birch, Finite Elastic Strain of Cubic Crystals, *Phys. Rev.* **71**, 809 (1947).
- [46] F. D. Murnaghan, The Compressibility of Media under Extreme Pressures, *Proc. Natl. Acad. Sci. USA* **30**, 244 (1944).
- [47] J. Heyd, G. E. Scuseria, and M. Ernzerhof, Hybrid functionals based on a screened Coulomb potential, *J. Chem. Phys.* **118**, 8207 (2003).
- [48] J. Heyd, G. E. Scuseria, and M. Ernzerhof, Erratum: “Hybrid functionals based on a screened Coulomb potential” [*J. Chem. Phys.* 118, 8207 (2003)], *J. Chem. Phys.* **124**, 219906 (2006).
- [49] A. V. Krugau, O. A. Vydrov, A. F. Izmaylov, and G. E. Scuseria, Influence of the exchange screening parameter on the performance of screened hybrid functionals, *J. Chem. Phys.* **125**, 224106 (2006).
- [50] D. E. Vanpoucke and K. Haenen, Revisiting the neutral C-vacancy in diamond: Localization of electrons through DFT+U, *Diam. Relat. Mater.* **79**, 60 (2017).
- [51] K. Boldyrev, B. Mavrin, P. Sherin, and M. Popova, Bright luminescence of diamonds with ge-v centers, *J. Lumin.* **193**, 119 (2018).
- [52] R. F. W. Bader, A Quantum Theory of Molecular Structure and Its Applications, *Chem. Rev.* **91**, 893 (1991).
- [53] R. G. Parr, P. W. Ayers, and R. F. Nalewajski, What Is an Atom in a Molecule?, *J. Phys. Chem. A* **109**, 3957 (2005).
- [54] P. Bultinck, C. Van Alsenoy, P. W. Ayers, and R. Carbó-Dorca, Critical analysis and extension of the Hirshfeld atoms in molecules, *J. Chem. Phys.* **126**, 144111 (2007).
- [55] D. E. P. Vanpoucke, P. Bultinck, and I. Van Driessche, Extending Hirshfeld-I to bulk and periodic materials, *J. Comput. Chem.* **34**, 405 (2013).
- [56] D. E. P. Vanpoucke, I. Van Driessche, and P. Bultinck, Reply to ‘Comment on “Extending Hirshfeld-I to bulk and periodic materials” ’, *J. Comput. Chem.* **34**, 422 (2013).
- [57] J. J. Wolffis, D. E. Vanpoucke, A. Sharma, K. V. Lawler, and P. M. Forster, Predicting partial atomic charges in siliceous zeolites, *Microporous Mesoporous Mater.* **277**, 184 (2019).
- [58] E. Bosoni, L. Beal, M. Bercx, P. Blaha, S. Blügel, J. Bröder, M. Callsen, S. Cottenier, A. Degomme, V. Dikan, K. Eimre, E. Flage-Larsen, M. Fornari, A. Garcia, L. Genovese, M. Giantomassi, S. P. Huber, H. Janssen, G. Kastlunger, M. Krack, G. Kresse, T. D. Kühne, K. Lejaeghere, G. K. H. Madsen, M. Marsman, N. Marzari, G. Michalíček, H. Mirhosseini, T. M. A. Müller, G. Petretto, C. J. Pickard, S. Poné, G.-M. Rignanese, O. Rubel, T. Ruh, M. Sluydts, D. E. P. Vanpoucke, S. Vijay, M. Wolloch, D. Wortmann, A. V. Yakutovich, J. Yu, A. Zadoks, B. Zhu, and G. Pizzi, How to verify the precision of density-functional-theory implementations via reproducible and universal workflows, *Nat. Rev. Phys.* **6**, 45 (2024).
- [59] D. E. P. Vanpoucke, HIVE-tools v4.x, <https://github.com/DannyVanpoucke/HIVE4-tools> (2019).
- [60] A. D. Becke, A multicenter numerical integration scheme for polyatomic molecules, *J. Chem. Phys.* **88**, 2547 (1988).
- [61] V. I. Lebedev and D. Laikov, Quadrature formula for the sphere of 131-th algebraic order of accuracy, *Doklady Mathematics* **59**, 477 (1999).
- [62] P. Pobedinskas, G. Degutis, W. Dexters, J. D’Haen, M. Van Bael, and K. Haenen, Nanodiamond seeding on plasma-treated tantalum thin films and the role of surface contamination, *Appl. Surf. Sci.* **538**, 148016 (2021).
- [63] K. N. Boldyrev, V. S. Sedov, D. E. Vanpoucke, V. G. Ralchenko, and B. N. Mavrin, Localized vibrational modes of GeV-centers in diamond: Photoluminescence and first-principles phonon study, *Diam. Relat. Mater.* **126**, 109049 (2022).
- [64] T. Iwasaki, F. Ishibashi, Y. Miyamoto, Y. Doi, S. Kobayashi, T. Miyazaki, K. Tahara, K. D. Jahnke, L. J. Rogers, B. Naydenov, F. Jelezko, S. Yamasaki, S. Nagamachi, T. Inubushi, N. Mizuochi, and M. Hatano, Germanium-Vacancy single color centers in Diamond, *Sci. Rep.* **5**, 12882 (2015).
- [65] D. E. P. Vanpoucke, K. Lejaeghere, V. V. Speybroeck, M. Waroquier, and A. Ghysels, Mechanical Properties from Periodic Plane Wave Quantum Mechanical Codes: The Challenge of the Flexible Nanoporous MIL-47(V) Framework, *J. Phys. Chem. C* **119**, 23752 (2015).
- [66] D. E. Vanpoucke, S. S. Nicley, J. Raymakers, W. Maes, and K. Haenen, Can europium atoms form luminescent centres in diamond: A combined theoretical–experimental study, *Diam. Relat. Mater.* **94**, 233 (2019).
- [67] A. Gali and J. R. Maze, Ab initio study of the split silicon-vacancy defect in diamond: Electronic structure and related properties, *Phys. Rev. B* **88**, 235205 (2013).
- [68] G. Thiering and A. Gali, Spin–orbit coupling and Jahn–Teller effect in  $T_d$  symmetry: an ab initio study on the substitutional nickel defect in diamond, *Philos. Trans. R. Soc. A* **382**, 20220310 (2023).
- [69] For the smallest super cell, this shift was 0.97 eV for the three optimisation strategies.
- [70] J. P. Perdew and K. Schmidt, Jacob’s ladder of density functional approximations for the exchange–correlation energy, *AIP Conference Proceedings* **577**, 1 (2001).



- [71] Since the HSE06 calculations are performed using the PBE geometries, there is a small offset with regard to the true HSE06 equilibrium volumes. As such, the EOS fitted pressure is not centered at 0 GPa. In addition, as the PBE supercells are optimized using an extended k-point set, an EOS fit on the total energies obtained for a  $\Gamma$ -only calculations (chosen for consistency between HSE06 and PBE results) presents a similar type of offset. Despite these offsets for the equilibrium configurations (*i.e.*, the middle point of each dataset), the qualitative and quantitative behaviour should be retained. We could also have chosen to present the results as function of the lattice parameter or volume change, expressed in %, in which case nicely aligned curves are obtained. However, this would prevent direct comparison with experimental data. Now however, relative changes in applied stress can directly be compared, considering one takes into consideration the offset of the equilibrium point.
- [72] B. Vindolet, M.-P. Adam, L. Toraille, M. Chipaux, A. Hilberer, G. Dupuy, L. Razinkovas, A. Alkauskas, G. m. H. Thiering, A. Gali, M. De Feudis, M. W. Ngandeu Ngambou, J. Achard, A. Tallaire, M. Schmidt, C. Becher, and J.-F. m. c. Roch, Optical properties of SiV and GeV color centers in nanodiamonds under hydrostatic pressures up to 180 GPa, *Phys. Rev. B* **106**, 214109 (2022).
- [73] This value was estimated based on the 8 and 50 GPa curves, presented in figure 2 of same paper:  $\sim 35 \text{ nm} / 42 \text{ GPa} = \sim 0.8 \text{ nm/GPa}$ .
- [74] E. A. Ekimov, S. G. Lyapin, A. A. Razgulov, and M. V. Kondrin, Ab initio Calculation of Impurity–Vacancy Complexes in Diamond at High Pressure, *J. Exp. Theor. Phys.* **129**, 855 (2019).
- [75] V. G. Ralchenko, V. S. Sedov, A. A. Khomich, V. S. Krivobok, S. N. Nikolaev, S. S. Savin, I. I. Vlasov, and V. I. Konov, Observation of the Ge-vacancy color center in microcrystalline diamond films, *Bull. Lebedev Phys. Inst.* **42**, 165 (2015).